Ligand Migration and Protein Fluctuations in Myoglobin Mutant L29W[†,‡]

Karin Nienhaus,[§] Andreas Ostermann,[||,⊥] G. Ulrich Nienhaus,[§,#] Fritz G. Parak,[||] and Marius Schmidt*[,||]

Department of Biophysics, University of Ulm, Albert-Einstein-Allee 11, 89081 Ulm, Germany, Physikdepartment E17, Technische Universität München, James Franck Strasse, and ZWE FRM-II, Technische Universität München, Lichtenbergstrasse 1, 85747 Garching, Germany, and Department of Physics, University of Illinois at Urbana-Champaign, 1110 West Green Street, Urbana, Illinois 61801

Received November 25, 2004; Revised Manuscript Received February 3, 2005

ABSTRACT: We have determined eight X-ray structures of myoglobin mutant L29W at various experimental conditions. In addition, infrared spectroscopic experiments are presented, which are discussed in the light of the X-ray structures. Two distinct conformations of the CO-ligated protein were identified, giving rise to two stretching bands of heme-bound CO. If L29W MbCO crystals are illuminated around 180 K, a deoxy species is formed. The CO molecules migrate to the proximal side of the heme and remain trapped in the so-called Xe1 cavity upon temperature decrease to 105 K. The structure of this photoproduct is almost identical to the equilibrium high-temperature deoxy Mb structure. If the temperature is cycled to increasingly higher values, CO recombination is observed. Three intermediate structures have been determined during the rebinding process. Efficient recombination occurs only above 180 K, the characteristic temperature for the onset of protein dynamics. Rebinding is remarkably slow because bulky residues His64 and Trp29 block important migration pathways of the CO molecule.

Proteins are biological macromolecules that perform diverse tasks in living systems. Their biological function is determined by conformational changes of different magnitude. A quantitative understanding of protein function requires insight into both structural and dynamic properties of the protein. Detailed investigations have as yet only been performed on selected model systems, the most popular one being myoglobin (Mb).[1] This small globular protein binds diatomic ligands such as oxygen (O_2), carbon monoxide (CO), and nitric oxide (NO) reversibly at the iron in the center of a heme cofactor (*1*). Theoretical (*2*) and experimental (*3*−*5*) studies supplemented by computer simulations have revealed an astonishing complexity in this apparently simple binding process.

Mössbauer experiments on the heme iron (see reviews in refs *6* and *7*) as well as incoherent neutron scattering experiments (*8*−*10*) have shown that the dynamics of Mb differs below and above a characteristic temperature T_c (around 180 K). Functionally important, slow diffusive motions are activated only above T_c.

Low-temperature flash photolysis experiments by Frauenfelder and co-workers have shown that the ligand binding process involves multiple intermediate states (*5*). Starting in 1994, X-ray cryocrystallography below 180 K revealed that the reaction intermediates arise from transient binding of ligands at well-defined docking sites within the protein matrix. The photolyzed ligands were observed not only at the initial docking site B on top of the heme group (*11*−*13*) but also in other locations within the protein (*14*−*16*), the internal cavities Xe1−4 (*17*), named after their ability to accommodate xenon atoms. The clearest results were not obtained on the wild-type protein, but on mutant proteins, where the distal leucine L29 had been replaced by bulky aromatic residues such as tryptophan (L29W, Figure 1) or tyrosine (*14*, *16*).

In recent years, the time-resolved X-ray diffraction technique has been developed into a tool (*18*−*21*) that allows monitoring ligand migration through the protein matrix in real time (*22*−*25*). Time-resolved crystallographic studies are experimentally challenging, and it is difficult to monitor very small subpopulations. In contrast, spectroscopic experiments are easier to perform and are sensitive to very small subpopulations, provided that a suitable marker exists to study ligand migration. The infrared absorbance bands of heme-bound (*26*−*28*) as well as photolyzed CO (*29*−*31*) depend strongly on the local environment of the ligand and thus provide a tool to track CO on its way through the protein matrix.

A detailed infrared spectroscopic study on ligand migration and binding performed on solution samples of Mb mutant L29W has shown that, in contrast to wild-type Mb, essentially all ligands can be photolyzed and trapped at intermediate docking sites within the protein (*30*). In the course of these investigations, it became clear that the interaction between the Trp29 indole side chain and the CO dipole produces large spectral changes in the bands of photolyzed

[†] This work was supported by the Deutsche Forschungsgemeinschaft (Grants Ni291/3 and SFB569 to G.U.N. and SFB533 to M.S.) and the Fonds der Chemischen Industrie.

[‡] Crystallographic coordinates of L29W metMb$_{RT}$, L29W Mb$_{RT}$, and L29W MbCO$_{RT}$ were deposited in the Protein Data Bank with accession codes 2blh, 2bli, and 2blj, respectively.

* To whom correspondence should be addressed. Telephone: +49-(0)89 289 12550. Fax: +49-(0)89 289 12548. E-mail: marius@hexa.e17.physik.tu-muenchen.de.

[§] Department of Biophysics, University of Ulm.

[||] Physikdepartment E17, Technische Universität München.

[⊥] ZWE FRM-II, Technische Universität München.

[#] Department of Physics, University of Illinois at Urbana-Champaign.

[1] Abbreviations: Mb, myoglobin; FTIR, Fourier transform infrared.

10.1021/bi047513t CCC: $30.25
Published on Web 03/11/2005

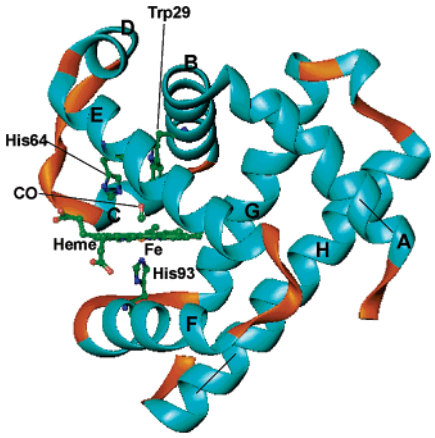

FIGURE 1: Ribbon representation of the overall structure of Mb mutant L29W (CO-ligated species). The helices are named according to standard convention. The heme plane, the CO ligand, active site residues His64 and Trp29, and the proximal His93 are included. This figure was created with Ribbons (*56*).

CO that could be used to unambiguously identify the location of the photodissociated ligands.

Here, we combine an X-ray diffraction study with infrared spectroscopy to provide direct structural information on the interplay between ligand migration and protein dynamics below and above T_c characteristic for the dynamical transition. We will show that ligand dissociation and migration lead to pronounced structural rearrangements at the active site that result in markedly smaller association rate coefficients in this mutant as compared to wild-type Mb.

MATERIALS AND METHODS

Sample Preparation. Mb mutant L29W was expressed in *Escherichia coli* and purified as described (*30*). Crystals were grown in 2.5 M $(NH_4)_2SO_4$, 20 mM Tris, and 1 mM EDTA, pH 8.5. X-ray structures were determined either at room temperature (RT; $T = 295$ K) or at low temperature (LT; $T = 105$ or 110 K). A crystal grown in the oxidized (Fe^{3+}, met) form was measured without further modification to obtain the room temperature structure, L29W metMb$_{RT}$. The reduced and unligated (deoxy) species, L29W Mb$_{RT}$, was prepared by equilibrating the ice-cold stabilization solution [2.6 M $(NH_4)_2SO_4$, 20 mM Tris, 1 mM EDTA], including a crystal for 45 min with N_2 gas. After addition of 5 μL of 1 M degassed sodium dithionite solution (5 mM final concentration) to reduce the heme iron, the vial was stored overnight on ice. Then the crystal was mounted in a capillary, one end of which was quickly sealed. To remove excess air from the capillary, 30 mL of N_2 gas was purged through needles which were glued airtight into the stainless steel reinforcement supporting the base of the capillary. The needles were abscised with pliers and sealed with epoxy. The capillaries were stored at room temperature. To obtain the CO-ligated form, L29W MbCO$_{RT}$, CO gas instead of N_2 was flushed through the stabilization buffer and the capillary. For comparison, the low-temperature L29W MbCO$_{LT}$ structure was determined at 110 K. Crystals were looped and immediately shock-frozen in liquid propane and stored in liquid nitrogen. For the temperature-cycling experiments, the mother liquor was exchanged stepwise over a period of 2 days by the same mother liquor containing 0.8 M trehalose in addition. The CO form was produced as described above, and crystals were shock-frozen directly in the liquid nitrogen cryostream.

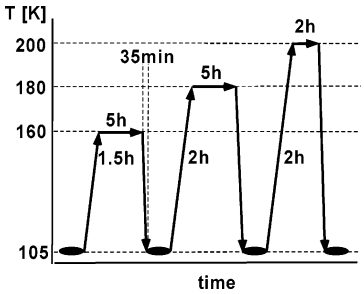

FIGURE 2: Temperature ramp protocol used to monitor sequential ligand recombination in L29W. Ellipses indicate X-ray data collection.

Fourier Transform Infrared (FTIR) Spectroscopy. A CO-ligated crystal (prepared as described above) was sandwiched between two CaF_2 windows separated by a 10 μm Mylar spacer and mounted inside a block of oxygen-free high-conductivity copper on the coldfinger of a closed-cycle helium refrigerator (model SRDK-205AW; Sumitomo, Tokyo, Japan). The temperature was adjusted with a digital temperature controller (model 330; Lake Shore Cryotronics, Westerville, OH). A continuous-wave, frequency-doubled Nd:YAG laser (model forte 530-300; Laser Quantum, Manchester, U.K.) was operated at 300 mW output at 532 nm to photolyze the crystalline sample. Transmission spectra were collected in the mid-IR (1800−2300 cm^{-1}, resolution 2 cm^{-1}) using a Fourier transform infrared (FTIR) spectrometer (IFS 66v/S; Bruker, Karlsruhe, Germany).

X-ray Crystallography: Data Acquisition. X-ray structures were measured on a FR-591 Enraf-Nonius rotating anode equipped with a HiStar multiwire gas detector (Bruker, Karlsruhe, Germany). To collect data on a photolyzed L29W MbCO crystal, the temperature of the cryostream was initially set to 150 K. Using a 50/50 beam splitter and mirrors, the L29W MbCO crystal was illuminated from opposite sides with 532 nm light from a continuous-wave frequency-doubled Nd:YAG laser (model forte 530-300; Laser Quantum, Manchester, U.K.). The size of the focus was 1 mm (full width at 1/e^2 of the peak intensity). The laser power was increased in steps until Debye−Scherrer rings showed up in the diffraction pattern at a laser power of 150 mW. They indicate a real crystal temperature of >180 K, as similar Debye−Scherrer rings started to appear at a temperature of 180 K without laser illumination, arising from a phase transition in the mother liquor. Subsequently, the laser power was slowly reduced to 100 mW (8 mW/min). With the laser power at 100 mW, the temperature of the cryostream was decreased to 105 K (0.25 K/min). Then, the laser power was further reduced to 30 mW at a rate of 1.4 mW/min. Data of the photolyzed L29W MbCO crystal were collected at 105 K and a laser power of 30 mW. The obtained structure is called L29W Mb$_{LT}$ in the following, which indicates a deoxy-like Mb structure.

After data acquisition, the laser was switched off, and the crystal was subjected to a temperature-cycling protocol to allow for sequential recombination (Figure 2). In a first step, the crystal was warmed to 160 K over a time period of 1.5 h and kept there for 5 h. Subsequently, the crystal was cooled to 105 K in 35 min, and data were collected. This moderate temperature increase is expected to allow for recombination

Table 1: Data Collection Statistics

	(a) Experiments at Thermal Equilibrium			
	L29W metMb$_{RT}$	L29W Mb$_{RT}$	L29W MbCO$_{RT}$	L29W MbCO$_{LT}$
temperature (K)	295	295	295	110
$a = b$, c (Å)	92.4, 46.8	91.8, 46.2	91.9, 46.0	91.1, 45.4
total observations	81268	99657	73405	66695
unique reflections	19497	21049	16299	20767
resolution (Å)	1.77	1.70	1.80	1.70
last shell (Å)	1.85−1.77	1.78−1.70	1.88−1.80	1.78−1.70
multiplicity (%) (last shell)	4.2 (1.8)	4.7 (2.0)	4.5 (2.5)	3.2 (1.9)
completeness (%) (last shell)	89.4 (51.0)	85.3 (73.1)	80.0 (61.0)	87.4 (71.7)
$I/\sigma(I)$ (last shell)	18.1 (4.2)	10.9 (2.8)	11.0 (3.0)	8.5 (4.2)
R_{sym} (%) (last shell)	3.0 (18.1)	5.1 (26.0)	5.3 (24.1)	5.8 (17.9)
R_{cryst}/R_{free} (%)	18.6/20.2	18.8/20.7	19.8/22.6	24.3/26.8
no. of water molecules	129	101	110	190
average B-factor (all atoms) (Å^2)	22.3	21.0	20.5	17.6
	(b) Photolysis Experiment			
	L29W Mb$_{LT}$ illumination >180 K, CO in Xe1	L29W Mb$_{160K}$ heat−cool cycle to 160 K	L29W Mb$_{180K}$ heat−cool cycle to 180 K	L29W Mb$_{200K}$ heat−cool cycle to 200 K
temperature (K)	105	105	105	105
$a = b$, c (Å)	90.41, 45.22	90.41, 45.22	90.41, 45.22	90.41, 45.22
total observations	182060	69134	73582	77376
unique reflections	29561	22242	20522	18584
resolution (Å)	1.55	1.70	1.75	1.80
last shell (Å)	1.60−1.55	1.76−1.70	1.81−1.75	1.86−1.80
multiplicity (%) (last shell)	6.2 (3.0)	3.1 (1.5)	3.6 (1.8)	4.2 (2.5)
completeness (%) (last shell)	96.2 (85.1)	95.3 (83.8)	95.8 (83.2)	94.3 (81.8)
$I/\sigma(I)$ (last shell)	13.0 (5.0)	18.5 (4.9)	14.4 (6.0)	17.1 (4.7)
R_{sym} (%) (last shell)	4.8	3.6	4.4	5.0
R_{cryst}/R_{free} (%)	19.4/22.3	19.6/22.4	19.4/22.3	20.2/23.6
no. of water molecules	187	184	181	181
average B-factor (all atoms) (Å^2)	10.0	12.1	11.6	12.3

of CO molecules with comparatively low rebinding barriers. In a second cycle, the crystal temperature was increased to 180 K over 2 h, kept constant for 5 h, and again decreased to 105 K for data collection. Finally, the temperature was raised to 200 K over 2.5 h, held there for 2 h to complete recombination, and then cooled for data collection. The structures generated after temperature cycling to 160, 180, and 200 K are called L29W Mb$_{160K}$, L29W Mb$_{180K}$, and L29W Mb$_{200K}$, respectively (see also Figure 2). We emphasize that structure determination of all three species was performed at 105 K.

Refinement of Equilibrium Structures. The intensities of the reflections were integrated and scaled with the program SAINT (Bruker, Karlsruhe, Germany). The subsequent data reduction was performed with the CCP4 programs SCALA and TRUNCATE (*32*). A compilation of the statistical values for data reduction and structural refinement is shown in Table 1.

For the refinement of the met form, the published low-temperature (105 K) L29W MbCO$_{105K}$ structure, PDB entry (*33*) 1DO1 (*16*), was used as a starting structure, with all water molecules and the CO ligand removed. A rigid body refinement was followed by 2500 K simulated annealing and conventional positional refinement. Water molecules were added to difference electron density features larger than 3.5σ in a first cycle. In the last cycle, features larger than 2.5σ were also considered. Individual B-factors were subsequently determined after conventional refinement of the water positions. The resulting structure was used as a start for all other structure refinements. Care was taken not to assign any additional ligand of the heme during the refinement cycles. After the last refinement cycle, the $F_o - F_c$ difference electron density close to the heme was inspected. Once density was found, it was interpreted either as H_2O or CO and refined conventionally, with the iron−ligand interactions switched off. All refinement was done in CNS (*34*).

In the L29W MbCO$_{RT}$ structure, we discovered some admixture of metMb by inspecting the $2F_o - F_c$ and $F_o - F_c$ difference electron density maps near the Trp29. Therefore, we allowed two conformations (met and CO-ligated) for His64 and Trp29 and their nearest neighbors. A final occupancy refinement yielded 70% MbCO and 30% L29W metMb$_{RT}$.

Refinement of Photoproduct Structures. The refinement was done using X-PLOR 3.1 (*35*) starting with the same L29W MbCO$_{105K}$ structure as above. Amino acids Trp29 and His64 and the CO molecule were removed from the model, and a first set of $2F_o - F_c$ and $F_o - F_c$ difference maps was calculated. Amino acids Trp29 and His64 were rebuilt manually using the program "O" (*36*). Subsequently, a 2500 K simulated annealing, conventional positional refinement, and individual B-factor refinement were performed. During the simulated annealing run, the coordinates of the water molecules were fixed. A new set of $2F_o - F_c$ and $F_o - F_c$ difference maps and simulated annealing omit maps for the residues of interest was calculated and inspected. The photoproduct structure served as the starting model for the three structures taken during the temperature-cycling protocol. For the refinement, no angle restraints were used for His93 and the CO molecule with respect to the heme plane. The bond restraints for the CO molecule and His93 as well as the pyrrole nitrogen bonds to the iron atom were weakened

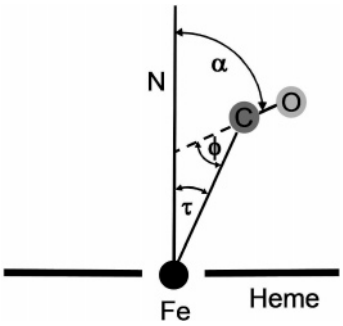

FIGURE 3: CO orientation with respect to the heme plane: N, heme normal; τ, tilt angle; ϕ, bend angle; α, tilt + bend.

from the standard X-PLOR values to allow for an almost unrestrained refinement in this region. After temperature cycling to 160 and 180 K, additional electron density appeared. This was accounted for by inserting those conformations of His64 and Trp29 into the electron density which are present in the unphotolyzed L29W $MbCO_{LT}$ structure. The occupancy values of these residues were determined for each temperature by a grouped occupancy refinement. In addition, the occupancy of the CO was determined at the proximal Xe1 site and at the iron binding site.

Relative Geometries and Electron Counts. The iron out-of-plane distance was determined with respect to the best-fit plane of the 20 porphyrin atoms. The normal of the heme plane was used to determine the tilt (τ) and, if applicable, the bend (ϕ) angles of the iron ligands (Figure 3). Structural changes are given relative to the L29W $metMb_{RT}$ structure, which serves as a reference. The normal on the Trp29 aromatic ring was determined with respect to a plane defined by three atoms of the ring. For each structure, the angular deviation of this normal was determined. In addition, the distance deviation Δd_{Trp29} with respect to the L29W $metMb_{RT}$ structure was calculated. For this purpose, the distances between all equivalent ring atoms were averaged. The His64 angle of deflection with respect to the met structure was computed with xfit (*37*) as the angle between the line connecting the His64-$N_{\epsilon 2}$ atom of a given structure and the His64-C_β atom of the L29W $metMb_{RT}$ structure and the line defined by His64-$N_{\epsilon 2}$ and His64-C_β of L29W $metMb_{RT}$. The distance deviation Δd_{His64} is equivalent to the displacement of the His64-$N_{\epsilon 2}$ atom. The number of electrons at the position of a putative ligand was determined from $mF_o - DF_c$ difference maps (*38*), which were calculated before the ligand was inserted in the density. To estimate the electron count, the difference density was integrated with the program "probe" (*21*). The result was multiplied by a factor of 2 to compensate for the fact that the difference electron density is represented on only half the absolute scale (*39*).

Structural distributions were assessed using the mean squared deviations of atomic positions, $\langle x^2 \rangle$, calculated from the temperature factors and averaged over backbone atoms using "moleman" (*40*). To examine structural differences, the atomic models were superimposed by aligning corresponding C_α atoms with the program "lsqman" (*40*).

RESULTS

FTIR Spectroscopy on L29W MbCO Crystals. The FTIR absorbance difference spectrum of the L29W MbCO crystal calculated from the transmission spectra collected before and after 1 s illumination at 3 K shows a dominant and a minor CO stretch band in the spectral region of heme-bound CO, denoted A_I (1945 cm^{-1}) and A_{II} (1958 cm^{-1}). They are associated with two discrete active site conformations (Figure 4). Photodissociated CO molecules trapped in the protein matrix give rise to a prominent IR band at ~2123 cm^{-1} and a minor band at 2131 cm^{-1}. Exposure to prolonged illumination, also performed at higher temperatures, enables ligands to sample intermediates with higher barriers opposing recombination (*41*, *42*). After extended illumination of the L29W MbCO crystal at temperatures below 180 K, photoproduct bands appeared at 2127 and 2133 cm^{-1}, whereas a band at 2130 cm^{-1} is observed after illumination at $T > 180$ K.

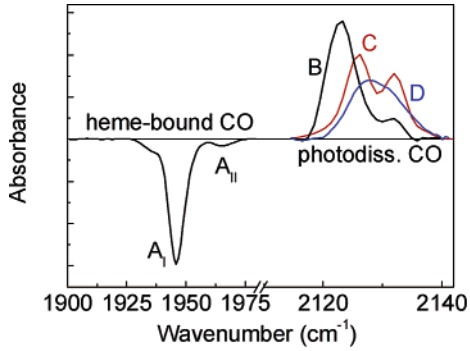

FIGURE 4: FTIR absorbance difference spectrum of a L29W MbCO crystal in the spectral regions of heme-bound and photolyzed CO, calculated from transmission spectra collected before and after 1 s illumination at 3 K (black, ligands at site B). Photoproduct spectra determined after extended illumination below (red, ligands at site C) and above (blue, ligands at site D) 180 K are included.

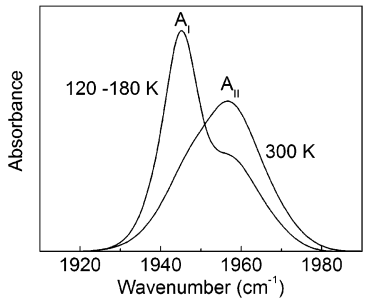

FIGURE 5: FTIR absorbance spectra of a L29W MbCO crystal at 120 and 300 K (the spectra between 120 and 180 K are identical). No cryoprotectant was added to the crystal. Corresponding X-ray structures: A_I, L29W $MbCO_{LT}$; A_{II}, L29W $MbCO_{RT}$.

A_I is the preferred state at low temperature. The A_{II} state gains at the expense of A_I with increasing temperature and accounts for essentially the total population at 300 K (Figure 5). Please note that, in Figure 5, we plot the absorbance spectra of the overall heme-bound CO, whereas Figure 4 shows only the subfraction that remains photolyzed long enough for data collection (200 s) after 1 s illumination at 3 K.

Equilibrium Structures at 295 and 110 K. Figure 6 shows the heme region for different oxidation and ligation states of the iron. In the reference structure L29W $metMb_{RT}$ (Figure 6A), a water molecule is coordinated to the heme iron ($Fe-H_2O$ distance of 2.2 Å). It is in optimal hydrogen bond distance to the $N_{\epsilon 2}$ of His64 (2.85 Å), whereas the distance to Trp29 is more than 3.5 Å (Table 2). In the deoxy form, no electron density can be detected at the position of the distal ligand (Figure 6B), indicating complete reduction. His64 is rotated by 25° toward the heme iron (see the L29W

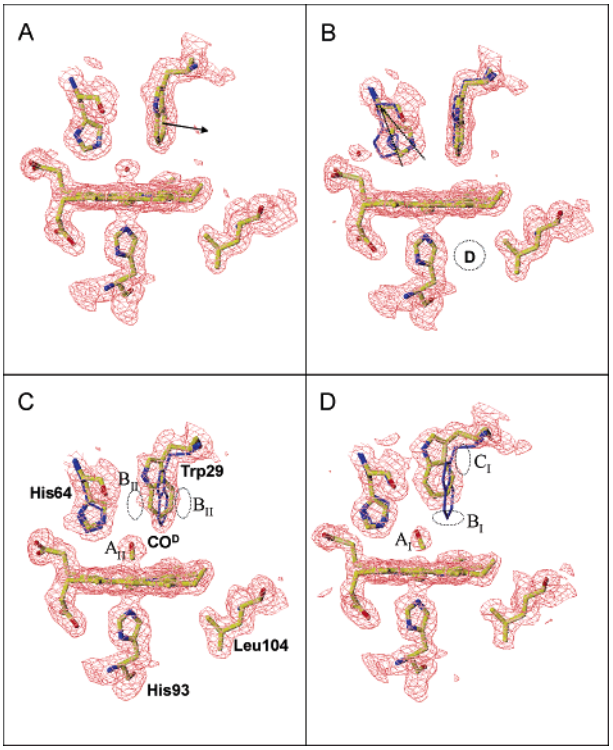

FIGURE 6: Equilibrium structures and $2mF_o - DF_c$ electron densities (1.2σ, orange) of the L29W Mb derivatives at the active site. Various CO docking sites B, C, and D are associated with the corresponding protein structure (explanation in the text). (A) Structure of L29W metMb$_{RT}$. Arrow: normal on the Trp29 aromatic ring. In (B−D), the structure of L29W metMb$_{RT}$ is shown as a reference in blue. (B) Structure of L29W Mb$_{RT}$. Dashed lines border the swing angle of His64. D: proximal CO binding site (Xe1 site). (C) Structure of L29W MbCO$_{RT}$. A_{II}: heme-bound CO in L29W MbCO$_{RT}$. B_{II}: putative primary docking sites in L29W MbCO$_{RT}$. (D) Structure of L29W MbCO$_{LT}$. A_I: heme-bound CO in L29W MbCO$_{LT}$. B_I: putative primary docking site in L29W MbCO$_{LT}$. C_I: secondary docking site in L29W MbCO$_{LT}$ (Xe4 site). This figure was created with the program O (*36*).

Mb$_{RT}$ structure in Figure 6B and Table 2). Additionally, a water molecule has bound to the $N_{\delta 1}$ of His64. Trp29 does not move; the heme adopts a domed conformation, with an iron out-of-plane distance of 0.37 Å.

Upon CO binding, the iron moves into the heme plane (Figure 6C, Table 2) and adopts a position similar to the one in L29W metMb$_{RT}$. His64 shifts to the position observed in the met structure. The distance between the oxygen of the CO and the His64-$N_{\epsilon 2}$ is 2.7 Å and thus 0.6 Å less than in wild-type MbCO (*43*, *44*), but roughly equivalent to the distances between the water oxygen and His64 in both wild-type and L29W metMb$_{RT}$. CO association also causes a conformational change of Trp29. This rearrangement was assessed by the angular deviation of the respective normals on the Trp29 aromatic rings and determined as 30° (Table 2). The spacing between the CO and Trp29-C_{H2} is 3.1 Å. It is comparable to the CO−Val68-$C_{\gamma 2}$ distance in wild-type MbCO, which might be considered as the minimum displacement between the ligand oxygen and an aliphatic carbon atom. Obviously, the CO is densely packed between His64 and Trp29. The CO stretches nearly perpendicular to the heme plane (see bend and tilt angles in Table 2). However, unless highest resolution data are available, the CO orientation should be taken with caution (compare discussion in refs *43* and *44*). To check for the occupancy of CO, we determined the integrated electron count at the position of the ligand. The presence of 13 electrons (see Table 2) corroborates full occupation of the ligand binding site. No additional CO binding sites were found.

Upon freezing of L29W MbCO crystals, an additional, slight structural change occurs (Figure 6D). Since the MbCO crystals frozen in propane (L29W MbCO$_{LT}$) and in the cryogenic nitrogen gas stream (L29W MbCO$_{105K}$) have identical structures, this conformational change does not depend on the freezing protocol. Apparently, CO-ligated protein adopts two conformations, depending on the temperature. Differences are observable close to Trp29. The normals on the Trp29 rings in L29W metMb and L29W MbCO$_{LT}$ differ by 38°. This value is about 10° larger compared to the one obtained for L29W MbCO$_{RT}$. The average displacement of the Tyr29 ring atoms toward the met structure is about 1.7 Å at 110 K, compared to 1.0 Å at room temperature. Notably, the geometry of the CO, established by the tilt and bend angles, is similar to the one observed at room temperature (Table 2). In addition, His64 moves slightly out of the distal pocket.

Photolysis Experiments. To break the bond between the heme iron and the ligand and to visualize the subsequent protein relaxation and ligand migration processes, the L29W MbCO crystal was illuminated at temperatures above 180 K. The electron density maps and structure models of the photoproduct states are shown in Figure 7. Substantial rearrangements with rms distances larger than 0.5 Å occur on the distal side of the heme pocket (Figure 7A, see His64 and Trp29), including the regions of the B-, C-, and E-helices as well as the C−D turn (Figure 8). The His64 side chain swings deeper into the heme pocket; the side chain of Trp29 rotates and matches the position observed in equilibrium L29W Mb$_{RT}$. As reported previously (*16*), electron density for the CO molecule appears in the Xe1 cavity (Figure 7A, CO^P). An occupancy refinement yields 50% of the CO molecules at the Xe1 site; less than 10% are bound at the heme iron (Table 3). The iron out-of-plane distance is 0.26 Å, a typical distance found in the deoxy conformation. The overall structure of this deligated species at 105 K is almost identical to the equilibrium room temperature structure L29W Mb$_{RT}$. Therefore, this photoproduct is called L29W Mb$_{LT}$. Another electron density feature close to the $N_{\delta 1}$ atom of His64 is modeled by a water molecule, which is also visible in the room temperature L29W Mb$_{RT}$ (Figure 7A, arrow).

Subsequently, we performed several temperature cycles to induce stepwise ligand recombination and protein relaxation back to the heme-bound state. When the temperature is increased to 160 K in the dark (Figure 7B), no significant structural changes of the protein are observed (L29W Mb$_{160K}$). The occupancy of the CO molecule in the Xe1 cavity decreases from 50% to 33%, and the fraction of heme-bound CO increases only slightly, from 7% to 11%. Structural changes of the protein set in after the temperature is increased to 180 K and, more pronounced, after the temperature is cycled to 200 K (panels C and D of Figure 7, respectively; see Trp29). The final structure (L29W Mb$_{200K}$, Figure 7D) is very similar to L29W MbCO$_{LT}$ obtained at 110 K under equilibrium conditions. The results of the occupancy refinements for the CO molecule, Trp29, and His64 as well as the electron density integration for the CO molecule are summarized in Table 3.

Table 2: Geometries of Selected X-ray Structures

		L29W Mb derivatives			
	L29W metMb$_{RT}$	L29W Mb$_{RT}$	L29W Mb$_{LT}$ (CO in Xe1)	L29W MbCO$_{RT}$	L29W MbCO$_{LT}$
temperature (K)	295	295	105	295	110
total structural deviation from L29W metMb$_{RT}$[a] (Å)		0.23	0.44	0.21	0.46
total electron count for ligand (e^-)[b]	9.6	<0.25		13.0	11.1
ligand occupancy (%)	96	<18		102[g]	79
iron out of plane (Å)	0.17	0.37	0.28	0.13	0.19
distance iron−His-N$_\epsilon$ (Å)	2.15	2.17	2.18	2.19	2.11
distance iron−ligand (Å)[c]	2.21			2.08	2.05
distance ligand−His64 (Å)[d]	2.85			2.69	2.87
distance ligand−Trp29 (Å)[e]	3.50			3.06	2.98
Trp29 normal relative to metMb (deg)		7.7	6.33	30.3	38.6
Δd_{W29}, Trp29 swing distance relative to metMb (Å)		0.10	0.10	1.0	1.71
Trp29 *B*-factor (main/side chain) (Å^2)	19.1/24.0	14.4/15.2	11.1/14.7	20.5/31.8	15.2/15.5
His64 rotation relative to metMb form (deg) positive: toward the solvent		−25.74	−27.77	−0.6	8.54
Δd_{H64}, His64-N$_{\epsilon 2}$ distance relative to metMb (Å)		−1.75	−1.80	−0.32	0.60
τ (tilt) (deg)	4.08			9.3	10.4
α ($\tau + \phi$) (deg)[f]				7.1	6.1

[a] Mean C$_\alpha$−C$_\alpha$ distance after least-squares fit. [b] Derived from integration of difference electron density. [c] Fe−C distance to CO in MbCO and Fe−O distance to H_2O in metMb. [d] Distance from the oxygen of either CO or H_2O to His64-N$_{\epsilon 2}$. [e] Distance from the oxygen of either CO or H_2O to Trp29-C$_{H2}$. [f] α = tilt (τ) plus bend (ϕ). [g] Assuming 30% metMb.

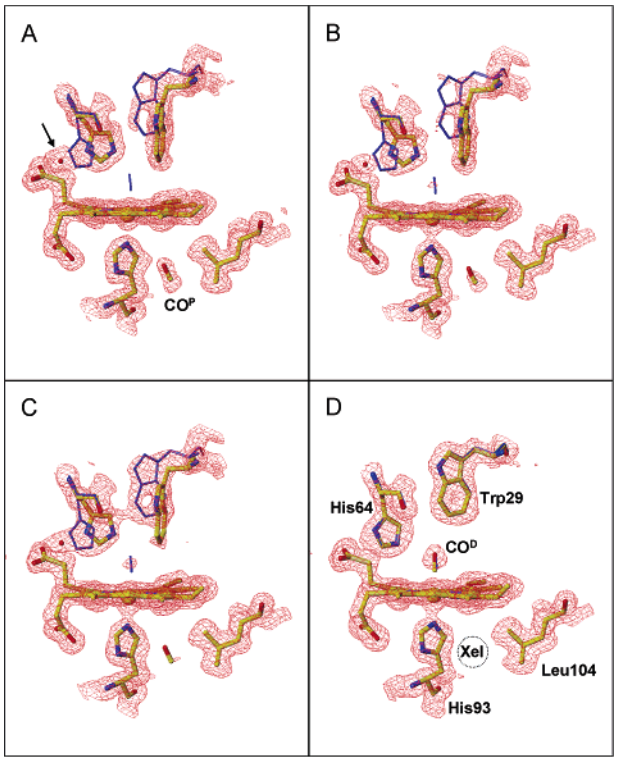

FIGURE 7: Structures and $2mF_o - DF_c$ electron densities (1.1σ, orange) near the heme of the photolysis experiment on L29W MbCO. The low temperature (110 K) structure L29W MbCO$_{LT}$ is shown in blue as a reference throughout. (A) $2mF_o - DF_c$ map of L29W Mb$_{LT}$ (105 K) after photolysis at 200 K. CO^P: proximal CO. The water molecule bound to the distal histidine is marked by the arrow. (B, C) $2mF_o - DF_c$ maps of the rebinding structures L29W Mb$_{160K}$ and L29W Mb$_{180K}$ after temperature cycling to 160 and 180 K. (D) $2mF_o - DF_c$ map of the rebinding structure L29W Mb$_{200K}$ after temperature cycling to 200 K. Amino acids His64, Trp29, Leu104, and His93 as well as the distal heme-bound CO (CO^D) and the position of the Xe1 site (site D) are marked.

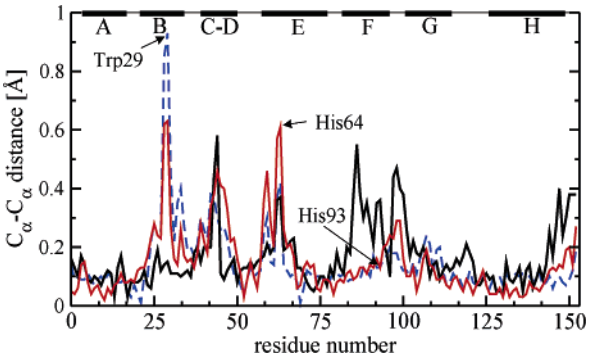

FIGURE 8: C$_\alpha$−C$_\alpha$ distances of equivalent residues in superimposed MbCO and deoxy-like structures at high and low temperatures. Solid red line: C$_\alpha$−C$_\alpha$ distances between L29W MbCO$_{RT}$ and L29W Mb$_{RT}$. Dashed blue line: C$_\alpha$−C$_\alpha$ distances between L29W MbCO$_{LT}$ and L29W Mb$_{LT}$ (with CO in Xe1). Solid black line: C$_\alpha$−C$_\alpha$ distances of wt MbCO (PDB entry 1A6G) and wt Mb (PDB entry 1A6N) at cryogenic temperatures (*44*).

DISCUSSION

Conformational Substates of Mb Mutant L29W. X-ray diffraction and FTIR experiments on Mb mutant L29W have revealed pronounced conformational changes upon ligand association and temperature variation. Three equilibrium conformations can be distinguished, a deoxy state, the structure of which is likely identical at all temperatures, and two distinct CO-bound conformations. The transition between the CO-ligated states involves marked conformational changes of residues His64 and Trp29 (Figure 6C,D), resulting in two stretching bands of heme-bound CO, A$_I$ at 1945 cm^{-1} and A$_{II}$ at 1960 cm^{-1}. As A$_{II}$ increases with temperature at the expense of A$_I$ (Figure 5), we propose that these absorbance bands identify the L29W MbCO$_{LT}$ (A$_I$) and L29W MbCO$_{RT}$ (A$_{II}$) structures. Compared to L29W metMb$_{RT}$, the A$_I$ state is represented by a strongly displaced and reoriented Trp29, and the A$_{II}$ state can be identified by a more moderately changed Trp29 orientation. In both substates, His64 is close to the position found in the met structure.

Figure 9, which has been adapted from ref *6*, illuminates the present results from another perspective. If wild-type MbCO is photolyzed at low temperatures, the CO ligand leaves the heme iron but the overall protein structure does not change (Figure 9A, left side). The CO may populate the

Table 3: Results from the Occupancy Refinement Using the Photolyzed Structures[a]

structure	CO in Xe1 (%)	heme-bound CO (%)	total CO identified (%)	His64, Trp29 Mb-like configuration (%)	His64, Trp29 MbCO configuration (%)
L29W Mb_{LT} (CO in Xe1)	50 (45)	7 (7)	57 (52)	77	23
L29W Mb_{160K}	33 (30)	12 (11)	45 (41)	74	23
L29W Mb_{180K}	26 (24)	32 (15)	58 (39)	51	45
L29W Mb_{200K}	12 (20)	68 (48)	80 (68)	16	79

[a] Results from the integration of CO electron density values are in parentheses (in %).

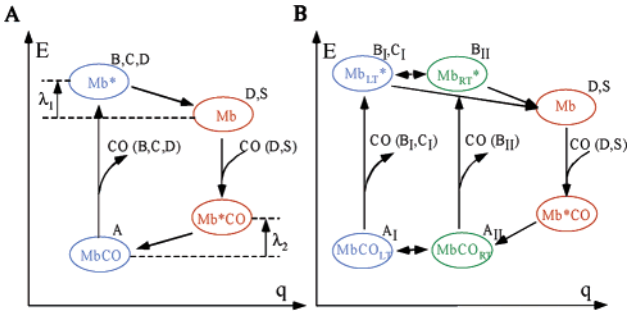

FIGURE 9: Photolysis experiments on wild-type and L29W MbCO (schematically). (A) Results from photolysis experiments on wild-type MbCO (for details see the text). Left side (in blue): MbCO-like structures. Right side (in red): deoxy-like structures. Site A: binding site of CO to the heme. Sites B, C (Xe4), D (Xe1), S (solvent): occupied by CO ligand after photolysis. (B) Results for the L29W mutant (for details see the text). Left side (in blue): MbCO-like structures populated preferentially at cryogenic temperatures. Middle (in green): MbCO-like conformations populated preferentially above T_c. Right side (in red): deoxy-like structures at $T > T_c$. Sites A_I, A_{II}: binding site of the CO to the heme in the different MbCO structures. Sites B_I, B_{II}, C_I (Xe4), D (Xe1), S (solvent): occupied by CO ligand after photolysis.

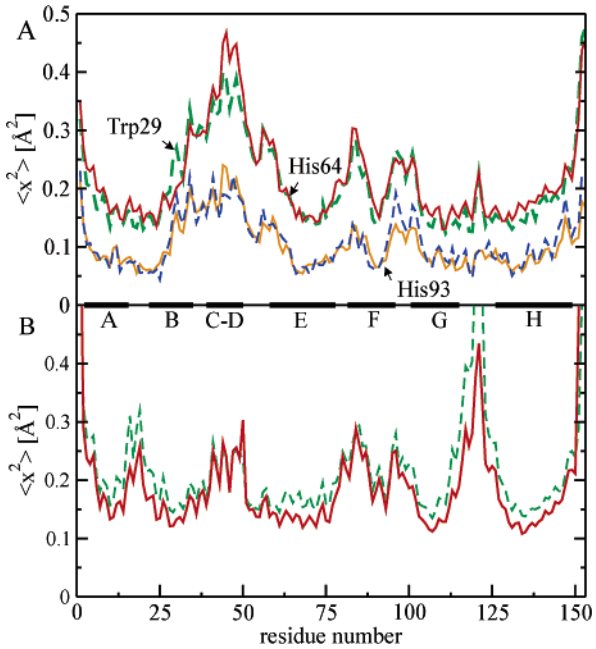

FIGURE 10: Mean squared displacements $\langle x^2 \rangle$ obtained from the backbone atoms of the L29W and wild-type Mb structures. Red (orange) lines are from deoxy-like structures, green lines from MbCO at room temperature, and blue lines from MbCO at cryogenic temperatures. (A) $\langle x^2 \rangle$ of the L29W myoglobin structures. Solid red line: L29W Mb_{RT}. Dashed green line: L29W $MbCO_{RT}$. Solid orange line: L29W Mb_{LT} (with CO in Xe1). Dashed blue line: L29W $MbCO_{LT}$. (B) $\langle x^2 \rangle$ of the wild-type myoglobin structures. Solid red line: wt Mb (PDB entry 1BZP). Dashed green line: wt MbCO (PDB entry 1BZR). Both at 287 K from ref *43*.

initial docking site B, as observed in low-temperature crystallography experiments (*11*−*13*). Docking site C (Xe4) was found by spectroscopy (*29*, *41*, *42*) but not by X-ray crystallography. The CO can migrate to the D (Xe1) position already below T_c in the wild type (*29*), but the protein stays rigid. Around T_c the protein relaxes toward the equilibrium deoxy structure (Figure 9A, right side). Photolyzed CO ligands may also escape from the molecule. Recombination of the CO from position D or S in the relaxed Mb occurs only above T_c via the transiently occupied state Mb*CO.

When Leu29 is mutated to Trp, the CO-ligated protein can adopt two structures, $MbCO_{LT}$ and $MbCO_{RT}$, where the indices RT and LT refer to room temperature and low temperature ($T < T_c$), respectively (Figure 9B). Both structures were associated with A_I and A_{II} by IR spectroscopy. Upon photolysis, Mb_{LT}* and Mb_{RT}* can be trapped below T_c. Only a minority of molecules are in Mb_{RT}* and the majority in Mb_{LT}*. Therefore, only the structure of Mb_{LT}* could be determined (*16*). It does not deviate from L29W $MbCO_{LT}$, except for minor changes in the iron region and that the CO is absent from the iron binding place. Analogically, we assume that the structure of Mb_{RT}* will likely be similar to that of L29W $MbCO_{RT}$. In a forthcoming paper, we will show structural relaxations of Mb_{RT}* at room temperature which happen on very short time scales. In Mb_{LT}* the photodissociated CO ligands are trapped in sites B_I at 3 K and C_I well below T_c. In Mb_{RT}* site B_{II} will be preferentially populated because the Tyr29 side chain blocks access to site B_I. Only above the characteristic temperature T_c do Mb_{LT}* and Mb_{RT}* molecules relax, and a single Mb structure accumulates. The CO escapes into the solvent or stays in site D (Xe1). This Mb structure was determined at room temperature and at 105 K and shown to be the same. Above T_c, recombination of the CO may occur either from the D site or from the outside of the molecule (site S). For the binding of CO to the iron to occur, both Trp29 and His64 have to fluctuate in order to open up the iron binding site. Large mean squared displacements of these residues (compare Figure 10) make this reasonable. There may be the possibility that these fluctuations locally generate His64 and Trp29 conformations also found in Mb_{LT}* and that just this conformation is functional. As a result, the association rate coefficient is markedly lower than that of wild-type Mb (see below). The structure of the Mb*CO could not be determined, but it is probably deoxy-like in analogy to the wild type. Finally, the protein relaxes back to the ground state, which is $MbCO_{RT}$ at $T > T_c$. Only a small fraction will adopt the $MbCO_{LT}$ conformation.

Proximal versus Distal Effects. Apart from the side chain conformations, the overall structural differences between L29W MbCO and L29W Mb are similar at high and low temperatures (Figure 8). The largest changes upon ligand

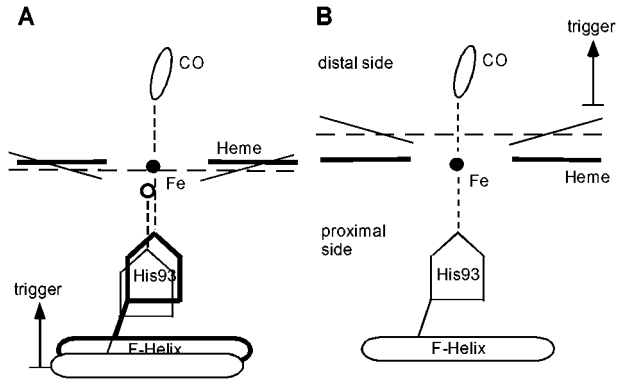

FIGURE 11: Proposed trigger mechanism for the structural changes from MbCO to deoxy in wild-type and L29W myoglobin (schematically). (A) wild type. After photodissociation of the CO, the iron moves out of the heme plane (long dashed line). The heme (thick solid line) domes to the proximal side (thin solid line). Both His93 and the F-helix move. (→) Trigger on the proximal side. (B) L29W mutant. The heme structure changes from the CO-bound form (thick solid line) to the deoxy-like structure (thin solid line) after CO is photodissociated. Although the heme is doming and the iron is out of plane (long dashed line), the iron as well as His93 and the F-helix do not move. (→) Trigger on the distal side.

association are observed in the B-helix in the vicinity of Trp29, the C−D turn, and the beginning of the E-helix including His64. The structural changes on the proximal side are much smaller than those on the distal side. This is in contrast to wild-type Mb (*43*, *44*) where some of the largest changes happen just at the F-helix on the proximal side of the heme plane (see also Figure 8).

In wild-type Mb, large-scale structural changes are triggered by the release of the ligand, including the doming of the heme plane toward the proximal side and the iron moving out of plane (Figure 11A) (*21*, *25*, *45*, *46*). In addition, the F-helix relocates. In the L29W mutant, however, we have observed a significant heme displacement toward the distal side (Figure 11B); the iron atom essentially retains its position. Consequently, the iron to His64-$N_{\epsilon 2}$ distance changes only on the order of a few hundredth of an ångstrom (Table 2). This holds for ambient and cryogenic temperatures. The structure is quite disordered near Trp29 in helix B and in the entire C−D region (Figure 8), where also the largest $\langle x^2 \rangle$ can be observed (Figure 10A). The heme group, by doming, may push the protein matrix on the distal side of the heme to a new conformation. This might also be the reason that Trp29 can adopt two slightly different conformations at low and high temperatures. In contrast, the proximal His93 has an especially low $\langle x^2 \rangle$, and conformational changes remain small on the proximal side in the mutant (compare Figure 10A and Figure 8). This is not observed in wild-type Mb, where the F-helix region actually has the largest $\langle x^2 \rangle$ of the entire globin (except for the loop connecting the G- and H-helix, which is disordered at room temperature) (Figure 10B).

Is this effect a result of crystal packing contacts? The mutant crystallizes in space group *P*6. The crystals contain about 60% water as compared with 32% in the wild-type protein (*47*). Therefore, one may expect that the mutant proteins are intrinsically more disordered in the crystal. However, crystal contacts, which are established just around residue 93 with the loop connecting helices G and H (around residue 120), may not only stabilize the loop (compare the $\langle x^2 \rangle$ values of wild-type Mb in Figure 10B with those of L29W shown in Figure 10A) but also prevent structural changes. Comparing the CO and deoxy forms of sperm whale Mb mutant D122N, which has the same structure as wild-type Mb and which also crystallizes in space group *P*6 [PDB entries 2MGK and 2MGL, respectively (*48*)], may provide the answer. Despite the *P*6 space group, the structural changes on the proximal side (data not shown in Figure 8) closely follow those observed in the wild-type protein with space group $P2_1$ (Figure 8A, black line). The lack of proximal structural changes likely results from the L29 mutation. Indeed, in triple mutant YQR (L29Y/H64Q/T67R), the most pronounced structural changes occur on the distal side (*24*), as in L29W.

Photoproducts in an A_I-Type Protein. At temperatures below 180 K, L29W MbCO molecules are preferentially in the A_I conformation (Figure 5). Brief illumination at 3 K breaks the bond between the CO and the heme iron, and the ligand migrates to the primary docking site B. Although no X-ray structure has been obtained at this temperature (3 K), the docking site B in substate A_I may be close to the site identified in wild-type Mb at cryogenic temperatures (*11*−*13*) because the CO stretching frequencies (B_2 at 2123 cm^{-1} and B_1 at 2131 cm^{-1}) are very similar to the ones observed in the wild-type protein (2119 and 2131 cm^{-1}). These two bands represent opposite orientations of the photolyzed ligands at site B and are caused by the so-called Stark effect, the interaction between the CO dipole and the local electric field at site B (*49*, *50*). If photolysis is performed at somewhat increased temperatures (*16*, *30*), essentially site C in the back of the distal pocket is populated. Site C has been identified as the Xe4 site behind Trp29 (see Figure 6D and ref *16*). In triple mutant YQR, both Tyr29 and Gln64 adopt positions equivalent to those of Trp29 and His64 in the A_I state (structure L29W $MbCO_{LT}$). After photolysis at 20 K, the CO ligands were also recovered in the Xe4 cavity (*14*). Subsequent FTIR experiments revealed that, in the YQR mutant, the thermally activated ligand migration process from B to C is already possible at temperatures as low as 20 K, whereas it needs ∼80 K in L29W (*16*), most likely due to the less voluminous Tyr29 side chain as compared to the indole side chain of Trp29 (*51*, *52*). Compared to the aliphatic Leu29 in wild-type Mb, both aromatic rings trap photolyzed ligands efficiently in the Xe4 cavity. Illumination at temperatures above 180 K (T_c) enables the photolyzed ligands to escape to the proximal Xe1 cavity. At the same time, however, the protein relaxes completely toward the deoxy structure (L29W Mb_{LT}).

Photoproducts in an A_{II}-Type Protein. At room temperature, the fraction of molecules in state A_{II} is increased at the expense of A_I (Figure 5). The local environment of the heme-bound CO is changed, shifting the CO stretching frequency from 1945 to 1960 cm^{-1}. This spectroscopic change might indicate a tighter packing of the CO. Indeed, in L29W $MbCO_{RT}$, the distances to His64 and Trp29 are slightly shorter compared to L29W $MbCO_{LT}$ (see Table 2). To identify X-ray structures of the A_{II} photoproduct states, we are essentially restricted to temperatures above 200 K. At these high temperatures, recombination is too fast to measure a photoproduct X-ray structure with conventional methods. However, even at cryogenic temperatures, a small fraction

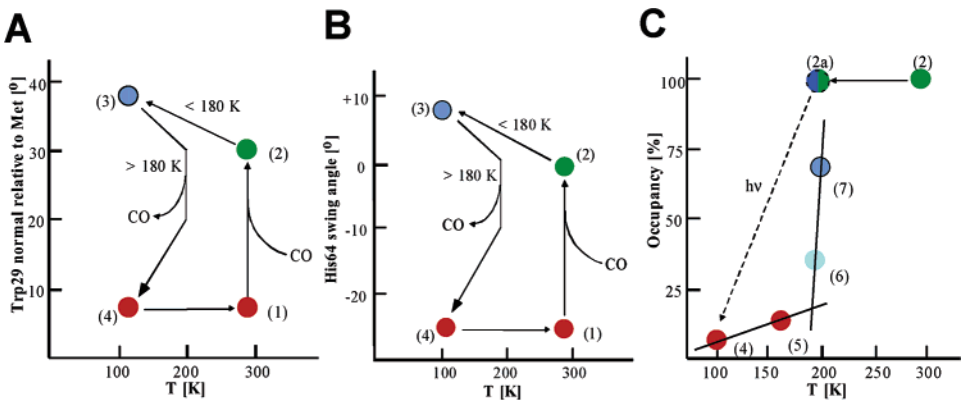

FIGURE 12: Properties of L29W myoglobin at several temperatures and ligation states. Green: MbCO structures at temperatures > T_c. Blue: MbCO structures measured at 105/110 K. Red: deoxy-like structures. (A) Changes in the Trp29 orientation as a function of temperature and coordination state of the heme iron. (1) L29W Mb_{RT}. (2) L29W $MbCO_{RT}$. (3) L29W $MbCO_{LT}$. The transition between (2) and (3) occurs most likely at 180 K. (4) L29W Mb with CO in Xe1. (4) can only be generated from (3) by illumination around or above 180 K. (B) Changes in the angle of His64 rotation as a function of temperature and coordination state of the heme iron. States are the same as in (A). (C) Occupancy values of the heme-bound CO as a function of temperature. (2) L29W $MbCO_{RT}$. (2a) L29W MbCO at 180 K (not determined; most likely a mixture of L29W $MbCO_{RT}$ and L29W $MbCO_{LT}$). (4) L29W Mb_{LT} with CO in Xe1. (5), (6), (7) Rebinding experiments of L29W Mb_{160K}, L29W Mb_{180K}, and L29W Mb_{200K}, respectively. CO-like structures emerge above the T_c at (6) and are fully occupied at (7). Two solid lines intersect at $T_c \sim 180$ K.

of the molecules is in the A_{II} conformation (Figure 4). With FTIR spectroscopy, it was possible to characterize intermediate docking sites for ligands in Mb molecules adopting conformation A_{II} (*30*). As the indole side chain most likely occludes the usual primary docking site, the location of the photolyzed ligands may coincide with one of the two initial positions observed in L29F Mb, between His64 and Phe29 (ref *23*; see also Figure 6C). No population was detected in the Xe4 cavity of A_{II} molecules, most likely because the rotation of the Trp29 side chain has reduced the open volume in Xe4. At temperatures above 180 K, photolyzed ligands migrate to site D and can be trapped there at cryogenic temperatures.

Interplay between Ligand Migration and Protein Relaxation. Panels A and B of Figure 12 summarize the observed structural changes of the L29W mutant with respect to temperature. If L29W MbCO is photodissociated at $T \sim 180$ K, the CO molecules leave the distal side and occupy the Xe1 site on the proximal side of the heme. Steady-state diffraction experiments on wild-type Mb (*15*) as well as time-resolved Laue experiments on wild-type Mb (*21*, *25*) and mutants L29F (*23*, *25*) and YQR (*24*) have also detected photolyzed ligands in Xe1. In L29W Mb, the voluminous indole side chain undergoes a pronounced relocation (Figure 12A, state 3 to 4), thereby efficiently occluding the primary photoproduct site. In addition, the His64 imidazole side chain rotates (Figure 12B, state 3 to 4) and covers the CO binding site at the heme iron. Hence, access of the CO to the iron is blocked by these two residues. This is the reason that markedly reduced ligand association rates are observed in L29W ($k'_{CO} = 0.0039\ \mu M^{-1}\ s^{-1}$, $k'_{O_2} = 0.29\ \mu M^{-1}\ s^{-1}$) as compared to wild-type Mb ($k'_{CO} = 0.51\ \mu M^{-1}\ s^{-1}$, $k'_{O_2} = 16\ \mu M^{-1}\ s^{-1}$) and L29F ($k'_{CO} = 0.20\ \mu M^{-1}\ s^{-1}$, $k'_{O_2} = 21\ \mu M^{-1}\ s^{-1}$) (*26*, *51*). The dissociation rate coefficients, by contrast, differ only slightly. Only for L29F MbO_2 is an ~10-fold decrease seen, because of more favorable interactions between the O_2 ligand and the distal residue Phe29 (*53*, *54*). In addition, a recent MD simulation suggests (*55*) that the dense side chain packing in the L29F mutant suppresses His64 fluctuations, thus inhibiting motions that can break the stabilizing hydrogen-bonding interaction of the His64-N_ϵ to the bound O_2 ligand.

To examine the interplay between protein dynamics and ligand migration from site D in more detail, we performed three successive heat−cool cycles and collected low-temperature data sets after each one (Figure 7). After a temperature increase to 160 K, the occupancy of the CO molecules in the proximal Xe1 cavity decreased slightly (Table 3), and no significant structural changes toward the L29W $MbCO_{LT}$ structure are detectable (Figure 7B) on the time scale of several days. Since site B is blocked by Trp29 and the iron binding site by His64 in L29W Mb_{LT}, recombination can only occur if these side chains transiently move away. Only above T_c are these fluctuations possible, and recombination takes place. In addition, transient channels open in the protein matrix, enabling the CO to migrate more freely. This prompts more and more CO molecules to exit the proximal Xe1 site or enter from the water space and to recombine at the heme iron (Figure 12C). Around 180 K, the onset of protein dynamics becomes evident, and the protein becomes functional. However, the occupancy values of the heme-bound CO and CO in the Xe1 site do not add up to 1.0 (see Table 3). About 40% of the CO molecules are not accounted for. Obviously, the molecules are distributed between multiple sites and also may have escaped the solvent. Their electron densities are too low at these sites so that their positions cannot be determined. The structure determination yields a mixture of the L29W $MbCO_{LT}$ and L29W Mb_{LT} conformations. If the temperature is increased further to 200 K, the protein relaxes completely to the L29W MbCO form; the structures are shown either in Figure 6C, D or in Figure 7D depending on the temperature. The intersection of the two solid lines in Figure 12C indicates the characteristic temperature T_c when this functional relaxation happens.

REFERENCES

1. Antonini, E., and Brunori, M. (1971) *Hemoglobin and Myoglobin in Their Reactions with Ligands*, North-Holland, Amsterdam.
2. Karplus, M., and Petsko, G. A. (1990) Molecular dynamics simulation in biology, *Nature 347*, 631−639.

3. Frauenfelder, H., and Wolynes, P. G. (1985) Rate theories and puzzles of hemeprotein kinetics, *Science 229*, 337−345.
4. Ansari, A., Berendzen, J., Braunstein, D., Cowen, B. R., Frauenfelder, H., Hong, M. K., Iben, I. E. T., Johnson, J. B., Ormos, P., Sauke, T. B., Scholl, R., Schulte, A., Steinbach, P. J., Vittitow, J., and Young R. D. (1987) Rebinding and relaxation in the myoglobin pocket, *Biophys. Chem. 26*, 337−355.
5. Austin, R. H., Beeson, K. W., Eisenstein, L., Frauenfelder, H., and Gunsalus, I. C. (1975) Dynamics of ligand binding to myoglobin, *Biochemistry 14*, 5355−5373.
6. Parak, F. (2003) Proteins in action: the physics of structural fluctuations and conformational changes, *Curr. Opin. Struct. Biol. 13*, 552−557.
7. Parak, F. (2003) Physical aspects of protein dynamics, *Rep. Prog. Phys. 66*, 103−129.
8. Doster, W., Cusak, S., and Petry, W. (1989) Dynamical transition of myoglobin revealed by inelastic neutron scattering, *Nature 337*, 754−756.
9. Bicout, D. J., and Zaccai G. (2001) Protein flexibility from the dynamical transition: a force constant analysis, *Biophys. J. 80*, 1115−1123.
10. Engler, N., Ostermann, A., Niimura, N., and Parak, F. (2003) Hydrogen atoms in proteins: position and dynamics, *Proc. Natl. Acad. Sci. U.S.A. 100*, 10243−10248
11. Schlichting, I., Berendzen, J., Phillips, G. N., Jr., and Sweet, R. M. (1994) Crystal structure of photolyzed myoglobin, *Nature 371*, 808−812.
12. Teng, T. Y., Srajer, V., and Moffat, K. (1994) Photolysis induced structural changes in single crystals of carbonmonoxy myoglobin at 40 K, *Nat. Struct. Biol. 1*, 701−705.
13. Hartmann, H., Zinser, S., Komninos, P., Schneider, R. T., Nienhaus, G. U., and Parak, F. (1996) X-ray structure determination of a metastable state of carbonmonoxy myoglobin after photodissociation, *Proc. Natl. Acad. Sci. U.S.A. 93*, 7013−7016.
14. Brunori, M., Vallone, B., Cutruzzola, F., Travaglini-Allocatelli, C., Berendzen, J., Chu, K., Sweet, R. M., and Schlichting, I. (2000) The role of cavities in protein dynamics: crystal structure of a photolytic intermediate of a mutant myoglobin, *Proc. Natl. Acad. Sci. U.S.A. 97*, 2058−2063.
15. Chu, K., Vojtechovsky, J., McMahon, B. H., Sweet, R. M., Berendzen, J., and Schlichting, I. (2000) Structure of a ligand-binding intermediate in wild-type carbonmonoxy myoglobin, *Nature 403*, 921−923.
16. Ostermann, A., Waschipky, R., Parak, F. G., and Nienhaus, G. U. (2000) Ligand binding and conformational motions in myoglobin, *Nature 404*, 205−208.
17. Tilton, R. F., Jr., Kuntz, I. D., Jr., and Petsko, G. A. (1984) Cavities in proteins: structure of a metmyoglobin-xenon complex solved to 1.9 Å, *Biochemistry 23*, 2849−2857.
18. Moffat, K. (1989) Time resolved macromolecular crystallography, *Annu. Rev. Biophys. Biophys. Chem. 18*, 309−232.
19. Schmidt, M., Pahl, R., Srajer, V., Anderson, S., Ren, Z., Ihee, H., Rajagopal, S., and Moffat, K. (2004) Protein kinetics: structures of intermediates and reaction mechanism from time-resolved X-ray data, *Proc. Natl. Acad. Sci. U.S.A. 101*, 4799−4804.
20. Perman, B., Anderson, S., Schmidt, M., and Moffat, K. (2000) New techniques in fast time-resolved structure determination, *Cell. Mol. Biol. 46*, 895−913.
21. Srajer, V., Ren, Z., Teng, T. Y., Schmidt, M., Ursby, T., Bourgeois, D., Pradervand, C., Schildkamp, W., Wulff, M., and Moffat, K. (2001) Protein conformational relaxation and ligand migration in myoglobin: nanosecond to millisecond molecular movie from time-resolved Laue X-ray diffraction, *Biochemistry 40*, 13802−13815.
22. Teng, T. Y., Srajer, V., and Moffat, K. (1997) Initial trajectory of carbon monoxide after photodissociation from myoglobin at cryogenic temperatures, *Biochemistry 36*, 12087−12100.
23. Schotte, F., Lim, M., Jackson, T. A., Smirnov, A. V., Soman, J., Olson, J. S., Phillips, G. N., Jr., Wulff, M., and Anfinrud, P. A. (2003) Watching a protein as it functions with 150ps time-resolved X-ray crystallography, *Science 300*, 1944−1947.
24. Bourgeois, D., Vallone, B., Schotte, F., Arcovito, A., Miele, A. E., Sciara, G., Wulff, M., Anfinrud, P., and Brunori, M. (2003) Complex landscape of protein structural dynamics unveiled by nanosecond Laue crystalllography, *Proc. Natl. Acad. Sci. U.S.A. 100*, 8704−8709.
25. Schotte, F., Soman, J., Olson, J. S., Wulff, M., and Anfinrud, P. A. (2004) Picosecond time-resolved X-ray crystallography: probing protein function in real-time, *J. Struct. Biol. 147*, 235−246.
26. Li, T., Quillin, M. L., Phillips, G. N., Jr., and Olson, J. S. (1994) Structural determinants of the stretching frequency of CO bound to myoglobin, *Biochemistry 33*, 1433−1446.
27. Phillips, G. N., Jr., Teodoro, M. L., Li, T., Smith, B., and Olson, J. S. (1999) Bound CO is a molecular probe of electrostatic potential in the distal pocket of myoglobin, *J. Phys. Chem. B 103*, 8817−8829.
28. Vogel, K. M., Kozlowski, P. M., Zgierski, M. Z., and Spiro, T. G. (1999) FeNO structure in distal pocket mutants of myoglobin based on resonance Raman spectroscopy, *J. Am. Chem. Soc. 121*, 9915−9921.
29. Nienhaus, K., Deng, P., Kriegl, J. M., and Nienhaus, G. U. (2003) Structural dynamics of myoglobin: effect of internal cavities on ligand migration and binding, *Biochemistry 42*, 9647−9658.
30. Nienhaus, K., Deng, P., Kriegl, J. M., and Nienhaus, G. U. (2003) Structural dynamics of myoglobin: spectroscopic and structural characterization of ligand docking sites in myoglobin mutant L29W, *Biochemistry 42*, 9633−9646.
31. Nienhaus, K., Deng, P., Olson, J. S., Warren, J. J., and Nienhaus, G. U. (2003) Structural dynamics of myoglobin: ligand migration and binding in valine 68 mutants, *J. Biol. Chem. 278*, 42532−42544.
32. Collaborative Computational Project, Number 4 (1994) The CCP4 suite: Programs for protein crystallography, *Acta Crystallogr. D50*, 760−763.
33. Berman, H. M., Battistuz, T., Bhat, T. N., Bluhm, W. F., Bourne, P. E., Burkhardt, K., Feng, Z., Gilliland, G. L., Iype, L., Jain, S., Fagan, P., Marvin, J., Padilla, D., Ravichandran, V., Schneider, B., Thanki, N., Weissig, H., Westbrook, J. D., and Zardecki, C. (2002) The Protein Data Bank, *Acta Crystallogr. D58*, 899−907.
34. Brunger, A. T., Adams, P. D., Clore, G. M., DeLano, W. L., Gros, P., Grosse-Kunstleve, R. W., Jiang, J. S., Kuszewski, J., Nilges, M., Pannu, N. S., Read, R. J., Rice, L. M., Simonson, T., and Warren, G. L. (1998) Crystallography & NMR system: A new software suite for macromolecular structure determination, *Acta Crystallogr. D54*, 905−921.
35. Bruenger, A. T. (1992) *X-PLOR, A System for X-ray Crystallography and NMR*, Yale University Press, New Haven, CT.
36. Jones, T. A., Zou, J. Y., Cowan, S. W., and Kjeldgaard, M.(1991) Improved methods for building protein models in electron density maps and the location of errors in these models, *Acta Crystallogr. A47*, 110−119.
37. McRee, D. E. (1999) XtalView/Xfit−A Versatile program for manipulating atomic coordinates and electron density, *J. Struct. Biol. 125*, 156−165.
38. Reed, R. (1986) Improved Fourier coefficients for maps using phases from partial structures with errors, *Acta Crystallogr. A42*, 140−149.
39. Henderson, R., and Moffat, J. K. (1971) The difference Fourier technique in protein crystallography and their treatment, *Acta Crystallogr. B27*, 1414−1420.
40. Kleywegt, G. J., and Jones, A. (1994) *Halloween ... masks and bones*, pp 59−66, SERC Daresbury, Warrington, U.K.
41. Nienhaus, G. U., Chu, K., and Jesse, K. (1998) Structural heterogeneity and ligand binding in carbonmonoxy myoglobin crystals at cryogenic temperatures, *Biochemistry 37*, 6819−6823.
42. Nienhaus, G. U., Mourant, J. R., Chu, K., and Frauenfelder, H. (1994) Ligand binding to heme proteins: the effect of light on ligand binding in myoglobin, *Biochemistry 33*, 13413−13430.
43. Kachalova, G. S., Popov, A. N., and Bartunik, H. D. (1999) A steric mechanism for inhibition of CO binding to heme proteins, *Science 284*, 473−476.
44. Vojtechovsky, J., Chu, K., Berendzen, J., Sweet, R. M., and Schlichting, I. (1999) Crystal structures of myoglobin-ligand complexes at near-atomic resolution, *Biophys. J. 77*, 2153−2174.
45. Martin, J. L., Migus, A., Poyart, C., Lecarpentier, Y., Astier, R., and Antonetti, A. (1983) Femtosecond photolysis of CO-ligated protoheme and hemeproteins: appearance of deoxy species with a 350fs time constant, *Proc. Natl. Acad. Sci. U.S.A. 80*, 173−177.
46. Franzen, S., Bohn, B., Poyart, C., and Martin, J. L. (1995) Evidence for sub-picosecond heme doming in hemoglobin and myoglobin: a time-resolved resonance Raman comparison of carbonmonoxy and deoxy species, *Biochemistry 34*, 1224−1247.
47. Parak, F., Hartmann, H., Schmidt, M., Corongiu, G., and Clementi, E. (1992) The hydration shell of myoglobin, *Eur. Biophys. J. 21*, 313−320.

48. Quillin, M. L., Arduini, R. M., Olson, J. S., and Phillips, G. N., Jr. (1993) High-resolution crystal structures of distal histidine mutants of sperm whale myoglobin, *J. Mol. Biol. 234*, 140−155.
49. Kriegl, J. M., Nienhaus, K., Deng, P., Fuchs, J., and Nienhaus, G. U. (2003) Ligand dynamics in a protein internal cavity, *Proc. Natl. Acad. Sci. U.S.A. 100*, 7069−7074.
50. Lim, M., Jackson, T. A., and Anfinrud, P. A. (1995) Mid-infrared vibrational spectrum of CO after photodissociation from heme: Evidence for a ligand docking site in the heme pocket of hemoglobin and myoglobin, *J. Chem. Phys. 102*, 4355−4366.
51. Lamb, D. C., Nienhaus, K., Arcovito, A., Draghi, F., Miele, A. E., Brunori, M., and Nienhaus, G. U. (2002) Structural dynamics of myoglobin: ligand migration among protein cavities studied by Fourier transform infrared/temperature derivative spectroscopy, *J. Biol. Chem. 277*, 11636−11644.
52. Lamb, D. C., Arcovito, A., Nienhaus, K., Minkow, O., Draghi, F., Brunori, M., and Nienhaus, G. U. (2004) Structural dynamics of myoglobin: an infrared kinetic study of ligand migration in mutants YQR and YQRF, *Biophys. Chem. 109*, 41−58.
53. Scott, E. E., Gibson, Q. H., and Olson, J. S. (2001) Mapping the pathways for O2 entry into and exit from myoglobin, *J. Biol. Chem. 276*, 5177−5188.
54. Carver, T. E., Brantley, R. E., Jr., Singleton, E. W., Arduini, R. M., Quillin, M. L., Phillips, G. N., Jr., and Olson, J. S. (1992) A novel site-directed mutant of myoglobin with an unusually high O_2 affinity and low autooxidation rate, *J. Biol. Chem. 267*, 14443−14450.
55. Hummer, G., Schotte, F., and Anfinrud, P. A. (2004) Unveiling functional protein motions with picosecond x-ray crystallography and molecular dynamics simulations, *Proc. Natl. Acad. Sci. U.S.A. 101*, 15330−15334.
56. Carson, M. (1991) Molecular display of simple molecules, proteins, nucleic acids, *J. Appl. Crystallogr. 24*, 958−961.

BI047513T